
Nasello et al., Bone, 2020 - Supplementary Material

1 MATHEMATICAL FORMULATION OF MECHANO-DRIVEN BONE REGENERATION

In this model, it is simulated a simultaneous process of cell invasion and bone formation regulated by the mechanical stimulus [1]. Cell invasion is treated as a diffusion process, according to Fick's law

$$\frac{\partial c}{\partial t} = D \cdot \frac{\partial^2 c}{\partial \underline{x}^2} \quad (S1)$$

where t and \underline{x} represent time and space, respectively. Cell concentration in the scaffold pores c is normalized to the maximum cell concentration, which is assumed to be in the surrounding bone tissue [2]. D is the diffusion constant, with no distinction between the single contributions of migrating cells and other cell types.

The role of mechanics on bone regulation is based on the effective tissue microstrain $\bar{\epsilon}$, calculated from the strain energy density W and the Young's modulus E [3]

$$\bar{\epsilon} = \sqrt{2 \cdot \frac{W}{E}} \cdot 10^6 \quad (S2)$$

The daily strain history depends on the strain levels and the load cases, which defines the daily strain stimulus for bone formation Ψ

$$\Psi = \sum_{i=1}^N (n_i \cdot \bar{\epsilon}^m)^{1/m} \quad (S3)$$

where N is the number of different daily load cases, n_i is the average number of daily cycles and m is a model parameter [4].

Mechanical stimulus regulates bone deposition by the remodeling error, which is the difference between the mechanical stimulus and a reference value [5]. In this model, the local daily strain stimulus Ψ_{local}^* in the peri-implant region is the reference value above which bone formation occurs [6]. The mathematical formulation of the bone volume deposition rate inside the pores of a bone scaffold

$$\dot{V} = \begin{cases} 0, & \text{if } \Psi \leq \alpha \cdot \Psi_{local}^* \\ k \cdot (\Psi - \alpha \cdot \Psi_{local}^*), & \text{if } \Psi > \alpha \cdot \Psi_{local}^* \\ \dot{V}_{max}, & \text{if } k \cdot (\Psi - \alpha \cdot \Psi_{local}^*) \geq \dot{V}_{max} \end{cases} \quad (S4)$$

assumes that:

- no bone resorption takes place for low mechanical stimuli [1]

- the daily strain stimulus initiating bone formation is reduced by a factor α (experimentally observed in the peri-implant region [7])
- bone formation is proportional to mechanical stimulus up to a maximum bone deposition rate \dot{V}_{max} [8].

Bone formation is intrinsically related to the increase of apparent mineral density and matrix mechanical properties. The apparent density rate $\dot{\rho}$ is the product of the cell concentration, the bone volume deposition rate and the maximum bone mineral density ρ_{max} [1]

$$\dot{\rho} = \bar{c} \cdot \dot{V} \cdot \rho_{max} \quad (S5)$$

Symbol	Meaning	Unit
c	Normalized cell concentration	<i>adimensional</i>
D	Diffusion constant	$\frac{cm^2}{s}$
W	Strain energy density	Pa
E	Young's modulus	Pa
$\bar{\epsilon}$	Effective tissue microstrain	$\mu\text{strains}$
Ψ	Daily strain stimulus for bone formation	$\mu\text{strains}$
N	Number of different daily load cases	<i>adimensional</i>
n_i	Average daily cycles	<i>adimensional</i>
m	Daily strain history parameter	<i>adimensional</i>
Ψ_{local}^*	Local daily strain stimulus in the peri-implant region	$\mu\text{strains}$
\dot{V}	Bone volume deposition rate inside the pores of a bone scaffold	$\frac{\% \left[\frac{mm^3_{bone}}{mm^3_{tissue}} \right]}{day}$
k	Constant of bone volume deposition rate	$\frac{\% \left[\frac{mm^3_{bone}}{mm^3_{tissue}} \right]}{\mu\text{strains} \cdot day}$
α	Fraction of reference daily stimulus	$\%$
\dot{V}_{max}	Maximum bone deposition rate	$\frac{\% \left[\frac{mm^3_{bone}}{mm^3_{tissue}} \right]}{day}$
$\dot{\rho}$	Bone mineral density rate	$\frac{g}{cm^3 \cdot day}$
ρ_{max}	Maximum bone mineral density	$\frac{g}{cm^3}$

Table S1. List of abbreviations and symbols in their order of usage in the text.

2 SUMMARY IN VIVO STUDY

Case	Week	Imaging technique		Bone ingrowth quantification				Pull-out
		CT	microCT	Femoral epiphysis	Femoral diaphysis	Tibial epiphysis	Tibial diaphysis	
1	12	×	×	●			●	●●●●
2	12	×	×	●		●		●●●●
3	12	×	×	●			●	●●●●
4	6		×	●	●			●●●●
5	6		×	●		●		●●●●
6	6		×	●		●		●●●●

Table S2. Detailed data of the *in vivo* test system. Summary of the *in vivo* data used to build and calibrate the computational model of bone ingrowth. 6 porous titanium scaffolds were implanted in the distal femur (3 scaffolds) and the proximal tibia (3 scaffolds) of 6 goats (cases), euthanized 6 or 12 weeks after implantation. Animals euthanized at week 12 received CT scanning, which were used to build the numerical simulations. For each animal, 2 samples were imaged by microCT scanning to quantify bone ingrowth within the scaffold pores in different locations of the femur and the tibia. The shear strength of the bone-scaffold interface was measured for 4 samples by means of a pull-out test.

3 NUMERICAL IMPLEMENTATION OF MECHANO-DRIVEN BONE REGENERATION

3.1 Block diagram

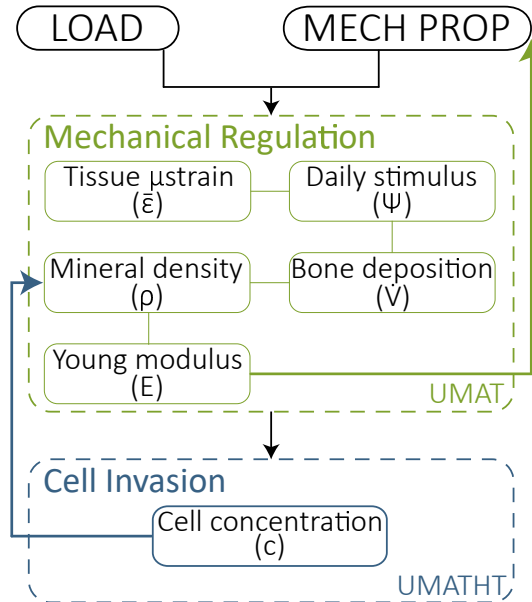


Figure S1. Block diagram of the bone regeneration algorithm. Using a coupled thermal-stress analysis, the algorithm sequentially implemented the concurrent processes of mechanical regulation and cell invasion described in the bone regeneration model. By means of Abaqus UMAT and UMATHT subroutines, cell concentration was extracted at each time step and used in the following step to compute the bone deposition rate due to mechanical regulation. Tissue mechanical properties were updated at the end of each step, thus changing the mechanical stimulus at each iteration.

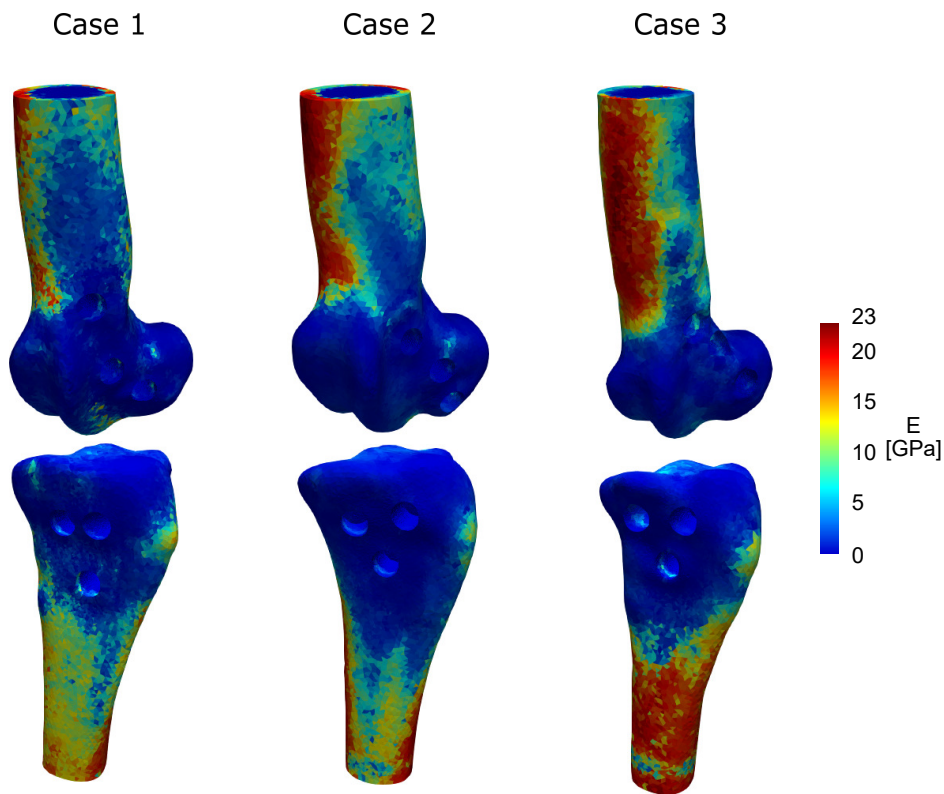
3.2 Material mapping

Mapping material properties on FE models means transforming Hounsfield units (HU) from CT images to mineral density values in the FE model. In this study, we used an empirical density–elasticity relationship expressed in terms of the apparent density (ρ_{app} , which is just ρ in the present document), as described by Morgan et al. [9]. However, CT scans provide only information about the bone mineral content, i.e. radiological density (ρ_{QCT}). Therefore, the workflow used to map material properties consisted of two main assumptions [10]:

- ρ_{QCT} (radiological density) was assumed equal to ash density (ρ_{ash});
- the established ρ_{ash} / ρ_{app} ratio of 0.6 was used to calculate ρ_{app} from ρ_{ash} [11]

Consequently, our procedure to extract the material properties was adapted as follows:

- HU were sampled from CT-scans of the goat;
- HU were converted to ρ_{QCT} , assumed equal to ρ_{ash} , using a linear pseudo-calibration;
- $\rho_{QCT} = \rho_{ash}$ was converted to ρ_{app} using the ratio previously reported (=0.6);
- $\rho_{app} = \rho$ was ultimately converted to Young’s modulus using the referenced relationships [12].



$$E \text{ (MPa)} = \begin{cases} 521.22 \cdot \rho^{0.43}, & \text{if } \rho < 0.9 \text{ g/cm}^3 \\ 65006.86 \cdot \rho - 58008.23, & \text{if } 0.9 \text{ g/cm}^3 \leq \rho \leq 1.2 \text{ g/cm}^3 \\ 17275.04 \cdot \rho^{0.80}, & \text{if } \rho > 1.2 \text{ g/cm}^3 \end{cases}$$

Figure S2. Bone material mapping. CT images HU were mapped onto the FE models, which were later pseudo-calibrated to transform HU into apparent density. Finally, bone material properties were assigned based on a continuous relationship between apparent density and modulus for ovine bone taken from the literature [12].

3.3 Mesh size

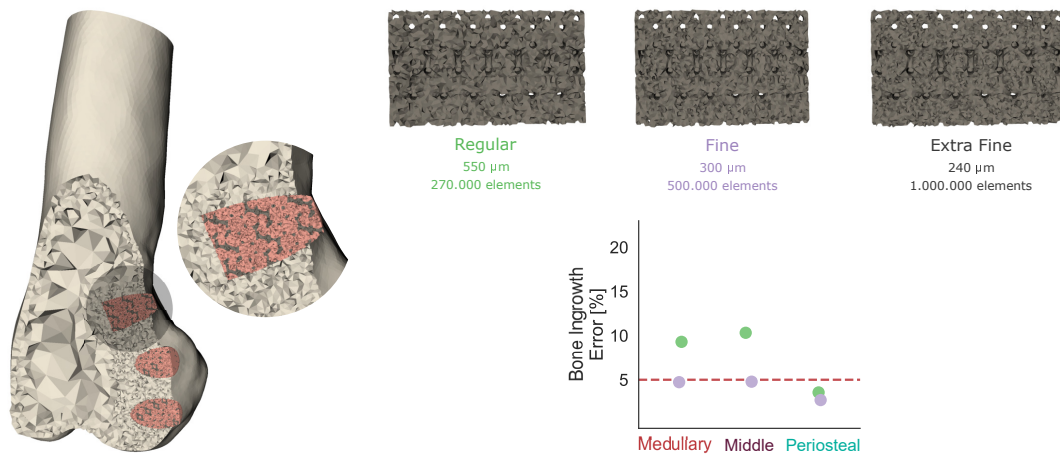


Figure S3. Influence of mesh size on numerical prediction. (A) Representative mesh of femoral *in silico* model and section detail of the scaffold-granulation unit. (B) Representative images of the three mesh sizes tested for the granulation domain. Below each image, the maximum edge length of the automatic meshing algorithm and the final number of elements are indicated. Prediction errors of bone ingrowth were computed for the regular and the fine mesh compared to the outcome of the extra fine mesh. Use of the fine mesh resulted in a numerical prediction of bone ingrowth that was within 5% error compared to the extra-fine mesh.

3.4 Boundary conditions

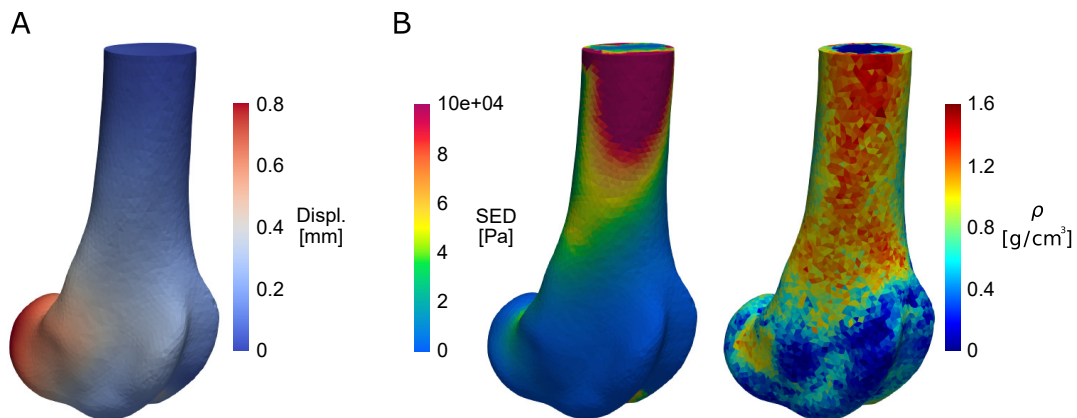


Figure S4. Effects of displacement constraints in the finite element model. (A) Representative femoral *in silico* model showing that absolute displacements were below 1mm throughout the model. (B) Strain energy density (SED) output of a finite element model with uniform mechanical properties of the femur (Young modulus of 1GPa, Poisson ratio of 0.3) and comparison with bone mineral density mapping extracted from CT images.

3.5 Parameter identification

Bone volume deposition rate											
$k \frac{\% \left[\frac{mm^3_{bone}}{mm^3_{tissue}} \right]}{\mu\text{strains} \cdot \text{day}}$											
$1 \cdot 10^{-5}$	$1.25 \cdot 10^{-5}$	$1.50 \cdot 10^{-5}$	$1.75 \cdot 10^{-5}$	$2 \cdot 10^{-5}$	$2.25 \cdot 10^{-5}$	$2.5 \cdot 10^{-5}$	$2.75 \cdot 10^{-5}$	$3 \cdot 10^{-5}$			
$3.25 \cdot 10^{-5}$	$3.50 \cdot 10^{-5}$	$3.75 \cdot 10^{-5}$	$4 \cdot 10^{-5}$	$4.25 \cdot 10^{-5}$	$4.5 \cdot 10^{-5}$	$4.75 \cdot 10^{-5}$	$5 \cdot 10^{-5}$	$5.25 \cdot 10^{-5}$			
$5.50 \cdot 10^{-5}$	$5.75 \cdot 10^{-5}$	$6 \cdot 10^{-5}$	$6.25 \cdot 10^{-5}$	$6.5 \cdot 10^{-5}$	$6.75 \cdot 10^{-5}$	$7 \cdot 10^{-5}$	$7.25 \cdot 10^{-5}$	$7.50 \cdot 10^{-5}$			
$7.75 \cdot 10^{-5}$	$8 \cdot 10^{-5}$	$8.25 \cdot 10^{-5}$	$8.5 \cdot 10^{-5}$	$8.75 \cdot 10^{-5}$	$9 \cdot 10^{-5}$	$9.25 \cdot 10^{-5}$	$9.5 \cdot 10^{-5}$	$9.75 \cdot 10^{-5}$			
$1 \cdot 10^{-4}$	$1.25 \cdot 10^{-4}$	$1.50 \cdot 10^{-4}$	$1.75 \cdot 10^{-4}$	$2 \cdot 10^{-4}$	$2.25 \cdot 10^{-4}$	$2.5 \cdot 10^{-4}$	$2.75 \cdot 10^{-4}$	$3 \cdot 10^{-4}$			
$3.25 \cdot 10^{-4}$	$3.50 \cdot 10^{-4}$	$3.75 \cdot 10^{-4}$	$4 \cdot 10^{-4}$	$4.25 \cdot 10^{-4}$	$4.5 \cdot 10^{-4}$	$4.75 \cdot 10^{-4}$	$5 \cdot 10^{-4}$	$5.25 \cdot 10^{-4}$			
$5.50 \cdot 10^{-4}$	$5.75 \cdot 10^{-4}$	$6 \cdot 10^{-4}$	$6.25 \cdot 10^{-4}$	$6.5 \cdot 10^{-4}$	$6.75 \cdot 10^{-4}$	$7 \cdot 10^{-4}$	$7.25 \cdot 10^{-4}$	$7.50 \cdot 10^{-4}$			
$7.75 \cdot 10^{-4}$	$8 \cdot 10^{-4}$	$8.25 \cdot 10^{-4}$	$8.5 \cdot 10^{-4}$	$8.75 \cdot 10^{-4}$	$9 \cdot 10^{-4}$	$9.25 \cdot 10^{-4}$	$9.5 \cdot 10^{-4}$	$9.75 \cdot 10^{-4}$			
Reduction factor											
α [%]											
1	2.5	5	7.5	10	12.5	15	17.5	20	25	30	35
40	45	50	55	60	65	70	75	80	90	95	100

Table S3. Range of parameters tested for fitting the *in vivo* results of bone ingrowth within porous titanium scaffold inserted in the distal femur and the proximal tibia of goat models. The constant of bone volume deposition rate k and the reduction factor α represent the mechano-sensitivity of the organism and the reduction of the reference stimulus initiating bone formation, respectively.

4 STATISTICAL ANALYSIS

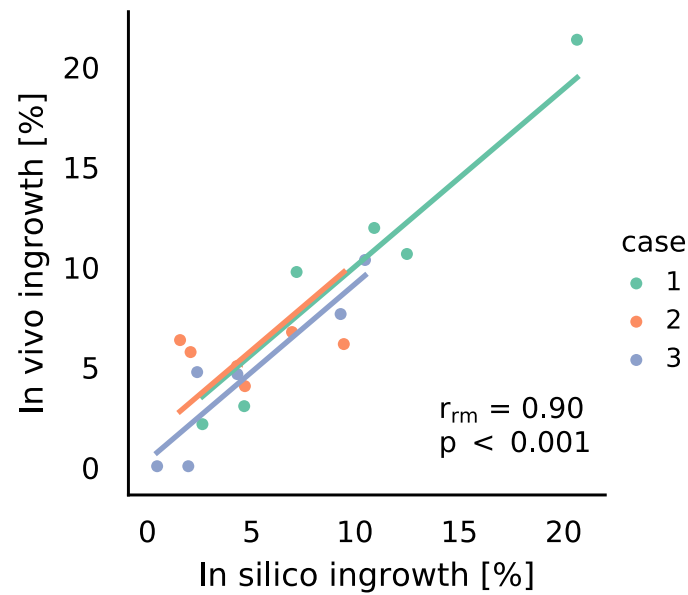


Figure S5. Repeated measure correlation (rmcorr) results for predicted (*in silico*) and experimental (*in vivo*) bone ingrowth data. Each dot represents bone ingrowth data in one of the medullary, middle and periosteal subregion of the scaffolds implanted in the left femurs and the tibiae of three different goats (cases). Observation from the same animal are given the same color, while lines show the individual rmcorr.

5 NUMERICAL OUTPUT

5.1 Local mechanical environment

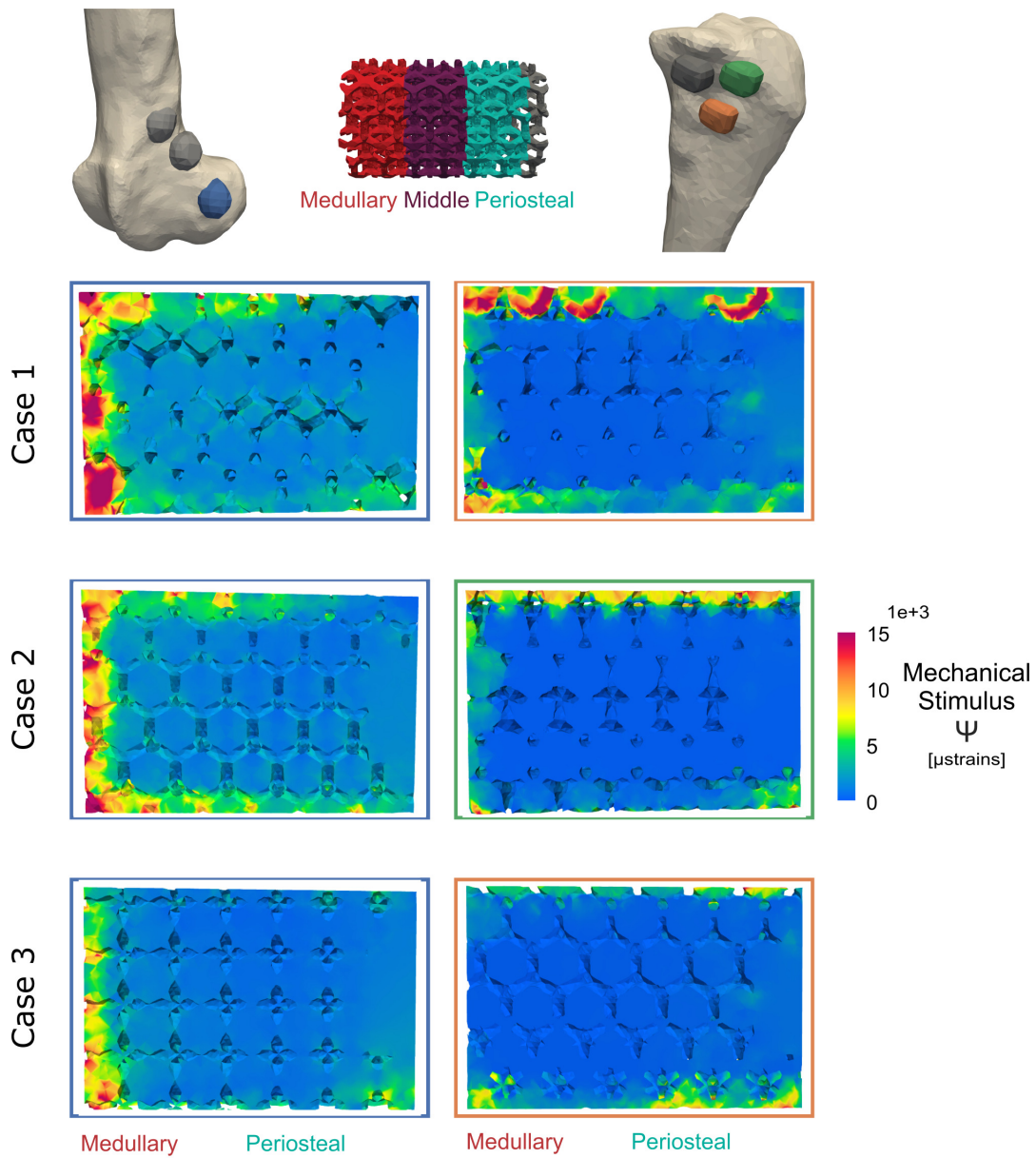


Figure S6. Local mechanical environment within the bone scaffolds at implantation time. Representative sections of the granulation domains at implantation time. Sections show the spatial distribution of the mechanical stimulus variable used in the mechano-driven model of bone regeneration (daily strain stimulus Ψ).

5.2 Output variability

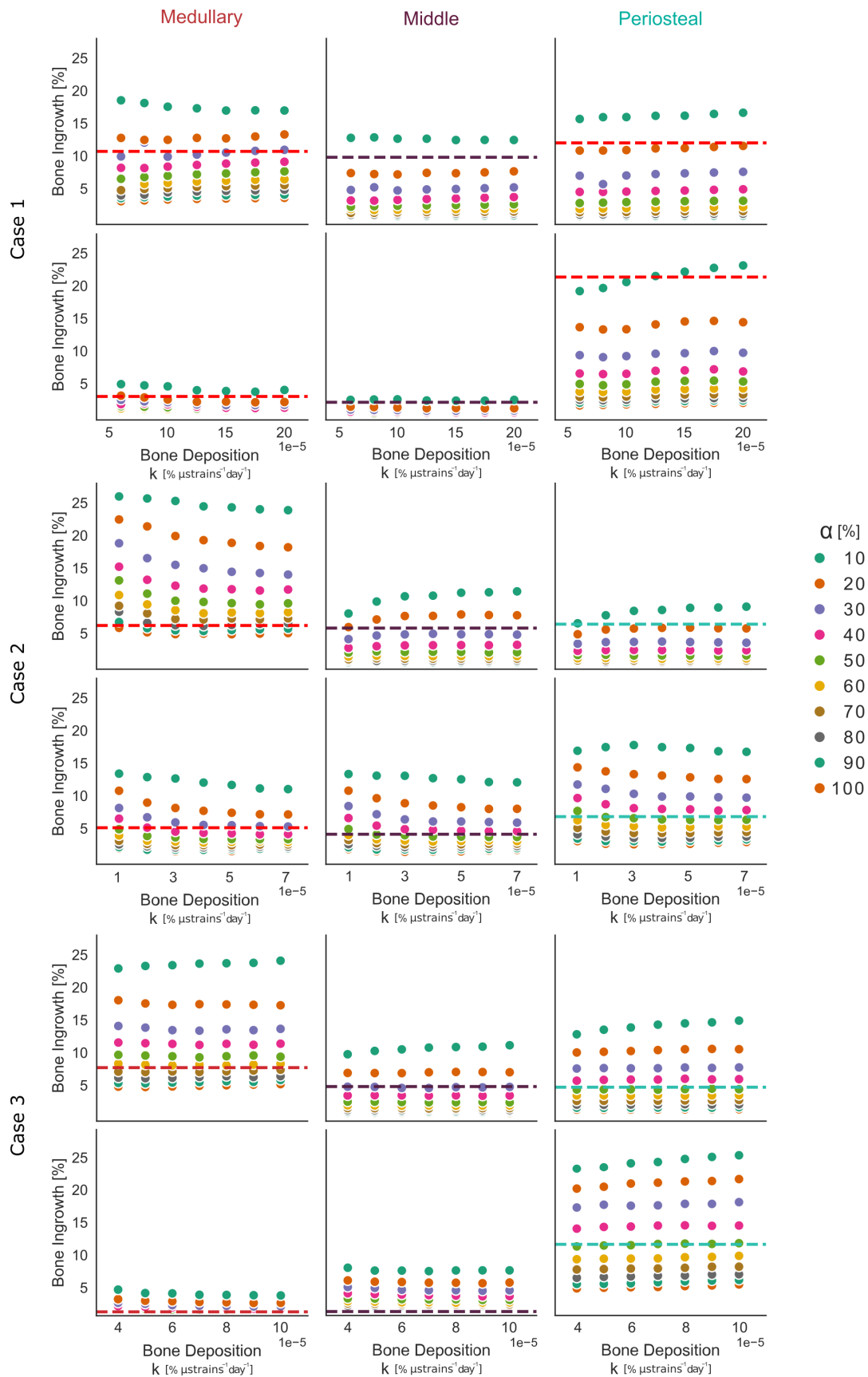


Figure S7. (Previous page.) Effect of tuning the constant of bone volume deposition k and the reduction factor α in the mechano-driven model of bone regeneration. Each row shows the variability in the bone ingrowth outcome predicted in the medullary, middle and periosteal subregions of a porous titanium bone scaffold when tuning k and α within a predefined range. A total number of six scaffolds was analyzed, two per goat (case). *In vivo* data of bone ingrowth in each subregion (dashed line in the plot) was used to estimate both k and α for each specific case and implantation site. To calibrate the model, parameters were selected based on the minimization of the residual sum of squares (RSS).

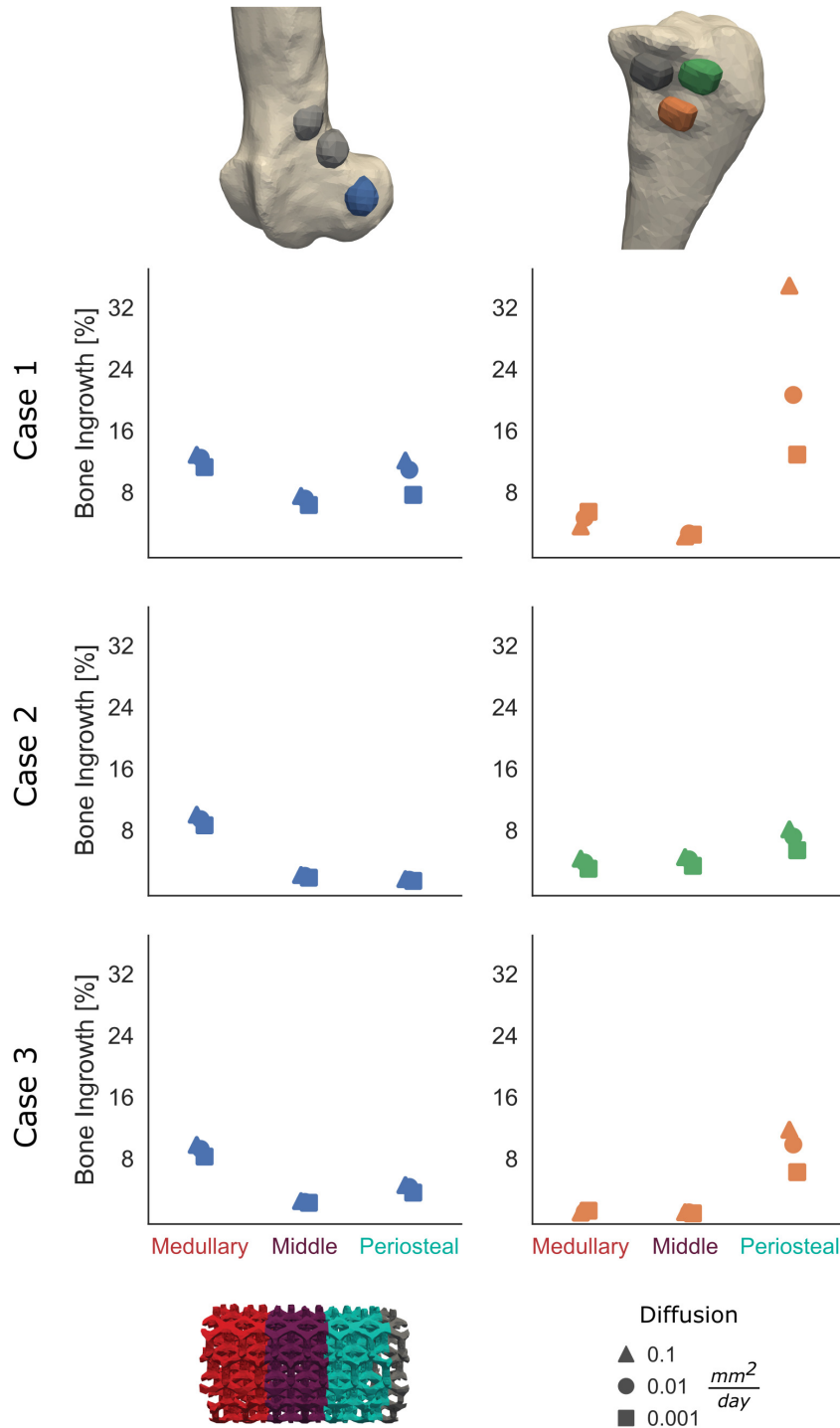


Figure S8. Effect of changing the diffusion constant D in the mechano-driven model of bone regeneration. Bone ingrowth was assessed in six different scaffolds inserted on the left femurs (continue next page)

Figure S8. (Previous page.) and the tibiae of three different goats (cases) after 12 weeks from implantation. Scaffolds were implanted in the epiphyseal (blue, green) and diaphyseal (orange) locations and bone ingrowth was quantified in the medullary (red), middle (purple) and periosteal (light blue) subregions. The mechano-driven model of bone regeneration was first calibrated while setting a cell diffusion constant D of $0.01 \text{ mm}^2/\text{day}$. Later, the computational analysis was repeated using a higher and a lower value of D , which covered the whole range of diffusion constants previously used in a bioregulatory model for bone healing [13].

5.3 Bone formation within the scaffold pores

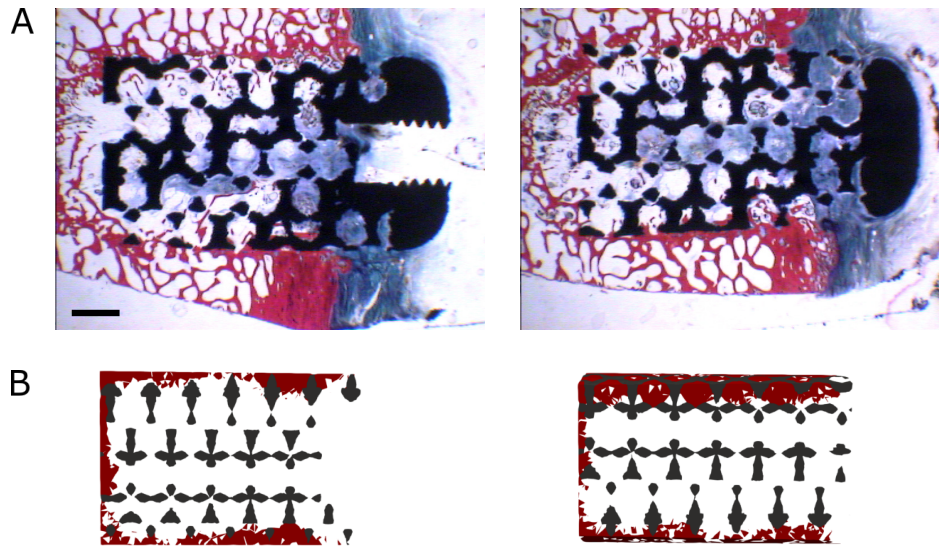


Figure S9. Novel formation of bone tissue in the outer scaffold pores. (A) Representative histological images and (B) numerical predictions showed bone tissue formation within the scaffold pores after 12 weeks from surgery. Both *in vivo* and *in silico* data reported limited bone ingrowth in the scaffold core. Scale bar, 20mm.

REFERENCES

- [1] J. A. Sanz-Herrera, J. M. García-Aznar, M. Doblaré, A mathematical model for bone tissue regeneration inside a specific type of scaffold, *Biomechanics and Modeling in Mechanobiology* 7 (5) (2008) 355–366. doi:10.1007/s10237-007-0089-7.
- [2] J. A. Sanz-Herrera, J. M. García-Aznar, M. Doblaré, On scaffold designing for bone regeneration: A computational multiscale approach, *Acta Biomaterialia* 5 (1) (2009) 219–229. doi:10.1016/J.ACTBIO.2008.06.021.
- [3] W. Pistoia, B. van Rietbergen, E.-M. Lochmüller, C. Lill, F. Eckstein, P. Rügsegger, Estimation of distal radius failure load with micro-finite element analysis models based on three-dimensional peripheral quantitative computed tomography images, *Bone* 30 (6) (2002) 842–848. doi:10.1016/S8756-3282(02)00736-6.
- [4] J. M. García-Aznar, T. Rueberg, M. Doblare, A bone remodelling model coupling microdamage growth and repair by 3D BMU-activity, *Biomechanics and Modeling in Mechanobiology* 4 (2-3) (2005) 147–167. doi:10.1007/s10237-005-0067-x.

- [5] D. R. Carter, G. S. Beaupré, Cancellous Bone, in: *Skeletal Function and Form*, Vol. 13, Cambridge University Press, 2000, pp. 138–160. doi:10.1017/CBO9780511574993.007.
- [6] T. Adachi, Y. Osako, M. Tanaka, M. Hojo, S. J. Hollister, Framework for optimal design of porous scaffold microstructure by computational simulation of bone regeneration, *Biomaterials* 27 (21) (2006) 3964–3972. doi:10.1016/j.biomaterials.2006.02.039.
- [7] Z. Li, D. Betts, G. Kuhn, M. Schirmer, R. Müller, D. Ruffoni, Mechanical regulation of bone formation and resorption around implants in a mouse model of osteopenic bone, *Journal of The Royal Society Interface* 16 (152) (2019) 20180667. doi:10.1098/rsif.2018.0667.
- [8] T. Adachi, Y. Kameo, M. Hojo, Trabecular bone remodelling simulation considering osteocytic response to fluid-induced shear stress., *Philosophical transactions. Series A, Mathematical, physical, and engineering sciences* 368 (1920) (2010) 2669–82. doi:10.1098/rsta.2010.0073.
- [9] E. F. Morgan, H. H. Bayraktar, T. M. Keaveny, Trabecular bone modulus–density relationships depend on anatomic site, *Journal of Biomechanics* 36 (7) (2003) 897–904. doi:10.1016/S0021-9290(03)00071-X.
URL <https://linkinghub.elsevier.com/retrieve/pii/S002192900300071X>
- [10] E. Schileo, F. Taddei, A. Malandrino, L. Cristofolini, M. Viceconti, Subject-specific finite element models can accurately predict strain levels in long bones, *Journal of Biomechanics* 40 (13) (2007) 2982–2989. doi:10.1016/j.jbiomech.2007.02.010.
URL <https://linkinghub.elsevier.com/retrieve/pii/S0021929007000711>
- [11] E. Schileo, F. Taddei, L. Cristofolini, M. Viceconti, Subject-specific finite element models implementing a maximum principal strain criterion are able to estimate failure risk and fracture location on human femurs tested in vitro, *Journal of Biomechanics* 41 (2) (2008) 356–367. doi:10.1016/j.jbiomech.2007.09.009.
- [12] S. Ghose, N. Reznikov, O. R. Boughton, S. Babu, K. C. Ng, G. Blunn, J. P. Cobb, M. M. Stevens, J. R. Jeffers, The design and in vivo testing of a locally stiffness-matched porous scaffold, *Applied Materials Today* 15 (2019) 377–388. doi:10.1016/j.apmt.2019.02.017.
- [13] L. Geris, A. Gerisch, J. V. Sloten, R. Weiner, H. V. Oosterwyck, Angiogenesis in bone fracture healing: A bioregulatory model, *Journal of Theoretical Biology* 251 (1) (2008) 137–158. doi:10.1016/J.JTBI.2007.11.008.